

PAPER • OPEN ACCESS

Atomic-scale identification of nitrogen dopants in graphene on Ir(111) and Ru(0001)

To cite this article: Huan Yang *et al* 2023 *J. Phys.: Condens. Matter* **35** 405003

View the [article online](#) for updates and enhancements.

You may also like

- [Quantum Energy Inequalities along stationary worldlines](#)
Christopher J Fewster and Jacob Thompson
- [Envisioning a sustainable agricultural water future across spatial scales](#)
Tara J Troy, Laura C Bowling, Sadia A Jame et al.
- [Highly sensitive detection of bacteria \(*E. Coli*\) Endotoxin using novel PANI-benzimidazole-Ag nanocomposite by DMMB dye displacement assay](#)
Tadele Ageru Alemu, Delele Worku Ayele, Shahitha Parveen J et al.

Atomic-scale identification of nitrogen dopants in graphene on Ir(111) and Ru(0001)

Huan Yang^{1,2,6}, Ivan Abilio^{3,4,6}, Juan Bernal Romero¹, Carlos Rodriguez¹, Miguel Escobar Godoy¹, Mitchell Little¹, Patrick Mckee¹, Vanessa Carbajal¹, Joey Li¹, Xing Chen¹, Hong-Jun Gao², Krisztián Palotás^{3,4,5,*}  and Li Gao^{1,*}

¹ Department of Physics and Astronomy, California State University, Northridge, CA 91330, United States of America

² Institute of Physics, Chinese Academy of Sciences, Beijing 100190, People's Republic of China

³ Institute for Solid State Physics and Optics, Wigner Research Center for Physics, H-1121 Budapest, Hungary

⁴ Department of Theoretical Physics, Institute of Physics, Budapest University of Technology and Economics, H-1111 Budapest, Hungary

⁵ ELKH-SZTE Reaction Kinetics and Surface Chemistry Research Group, University of Szeged, H-6720 Szeged, Hungary

E-mail: palotas.krisztian@wigner.hu and li.gao@csun.edu

Received 22 March 2023, revised 30 May 2023

Accepted for publication 27 June 2023

Published 7 July 2023



Abstract

Nitrogen (N) doped graphene materials have been synthesized using the sole precursor adenine on the Ir(111) and Ru(0001) surfaces. X-ray photoelectron spectroscopy and scanning tunneling microscopy (STM) have been used to characterize the obtained N-doped graphene materials. Several graphitic and pyridinic N dopants have been identified on the atomic scale by combining STM measurements and STM simulations based on density functional theory calculations.

Supplementary material for this article is available [online](#)

Keywords: nitrogen doped graphene, scanning tunneling microscopy, density functional theory calculations

(Some figures may appear in colour only in the online journal)

1. Introduction

Substitutional doping of graphene with heteroelements is one promising strategy for tuning the properties of graphene for

various applications [1, 2]. Nitrogen (N) doped graphene materials have potential applications in field-effect transistors, fuel cells, solar cells, lithium ion batteries, supercapacitors, sensors, photocatalysts, and gas storage [1–7]. Atomic-scale identification of N dopants in graphene can be achieved by combining scanning tunneling microscopy (STM) measurements and STM simulations based on density functional theory (DFT) calculations. Such combined studies have been performed to identify the N dopants in graphene on different supporting surfaces, such as SiC, SiO₂, Cu, and Ni [8–16]. Ir(111) and Ru(0001) are among the most commonly used supporting surfaces for graphene growth; however, the

⁶ H Y and I A contributed equally to this work.

* Author to whom any correspondence should be addressed.



Original content from this work may be used under the terms of the [Creative Commons Attribution 4.0 licence](#). Any further distribution of this work must maintain attribution to the author(s) and the title of the work, journal citation and DOI.

combined experimental and simulated STM studies have yet to be performed for N-doped graphene on these two transition metal surfaces. The free-standing graphene was used in most DFT calculations for comparing to STM images of N-doped graphene on the SiC, SiO₂, and Cu surfaces considering the weak graphene/substrate interaction [8, 10–15]. Some DFT calculations considered the supporting substrate for N-doped graphene on Ni(111) and Cu(111) with a flat graphene layer [9, 16]. The graphene layer is weakly corrugated on Ir(111) and strongly corrugated on Ru(0001), suggesting an increasing interaction between the graphene layer and these metal substrates. The DFT calculations of N-doped corrugated graphene on Ir(111) and Ru(0001) are not available so far. In addition, most of the DFT simulations of STM images for N-doped graphene have been focused on graphitic N and the simulations of pyridinic N dopants are very limited.

Here we report the synthesis of N-doped graphene on the Ir(111) and Ru(0001) surfaces using the sole precursor adenine. The bonding configurations of N dopants in the synthesized graphene materials are measured by using x-ray photoelectron spectroscopy (XPS). STM measurements and DFT calculations are combined to identify the bonding configurations of N dopants in corrugated graphene on these two metal surfaces with a focus on graphitic N and pyridinic N.

2. Experimental and theoretical methods

The growth experiments were performed using an ultrahigh vacuum (UHV) system with a base pressure lower than 2.0×10^{-10} Torr. The single crystal Ru(0001) surface (Princeton Scientific) was cleaned by repeated cycles of Ar⁺ ion sputtering (1.5 keV, 1.1×10^{-5} Torr, 30 min) at room temperature (RT), annealing at ~ 1500 K for 10 min, and subsequent flash annealing to ~ 1680 K. The single crystal Ir(111) surface (Princeton Scientific) was cleaned by repeated cycles of Ar⁺ ion sputtering (1.5 keV, 1.1×10^{-5} Torr, 40 min) at RT, annealing at ~ 1380 K for 10 min, annealing in oxygen (2.5×10^{-7} Torr) at ~ 1280 K for 20 min, flash annealing up to ~ 1500 K, annealing in hydrogen (5.0×10^{-7} Torr) at ~ 1280 K for 20 min, and flash annealing up to ~ 1500 K. The cleanness of the prepared metal surfaces was checked by using STM. The as-received adenine materials (Sigma-Aldrich) were thoroughly degassed in UHV prior to growth experiments. The deposition of adenine on metal surfaces was performed by thermal evaporation from an Al₂O₃ crucible. The metal surfaces were held at RT during precursor deposition. The growth of N-doped graphene was performed by annealing the precursor/metal sample up to 1173 K with a step of 100 K and a dwell time of 5 min at each temperature step. The Ir(111) and Ru(0001) surfaces act as the catalyst for the precursor cracking and graphene formation during the annealing process. The precursor deposition and subsequent thermal annealing compose one growth cycle. The coverage

of graphene on the metal surface increases with the number of growth cycles.

STM measurements were performed by using a Unisoku UHV low-temperature STM system (USM1500S) with a base pressure lower than 6.0×10^{-11} Torr. All of the STM measurements were carried out at 77 K with tungsten tips that were prepared by electrochemical etching and subsequently cleaned by thermal annealing in UHV. The STM images were recorded in a constant-current mode. For our STM, the tip is grounded and the bias voltage is applied to the sample. Therefore, an image recorded with a positive bias voltage is an empty-state image, and an image recorded with a negative bias voltage is a filled-state image. During the STM measurements of our samples, atomic-resolution was obtained sometimes with a tunneling current lower than 1 nA; however, often, a higher tunneling current up to 9 nA was used in order to achieve atomic resolution images or improve their quality. Atomic resolution STM images were usually recorded using a bias voltage of 500 mV or lower. XPS measurements were performed by using a Scienta Omicron XPS system with Mg x-ray source (1253.6 eV) and Argus CU (R) hemispherical electron energy analyzer. The binding energy (BE) scale was calibrated by using clean Au ($4f_{7/2} = 84.0$ eV BE). Peak fitting was carried out using the CasaXPS software.

DFT calculations were performed using the Vienna *Ab initio* Simulation Package [17, 18] with projector augmented waves [19], an energy cutoff of 400 eV, and van der Waals correction at the optB86b level [20, 21]. Supercell slabs are composed of three atomic layers of the metal fcc Ir(111) or hcp Ru(0001), followed by a single graphene overlayer in an asymmetric way. A separating vacuum region of at least 16 Å thickness was used to avoid unphysical interactions between the repeated image slabs in the perpendicular, Ir(111) or Ru(0001), direction. The bottom metal atomic layer was fixed and all other atoms were freely relaxed during the geometry optimizations, where the convergence criterion for the forces acting on individual atoms was set to 0.02 eV Å⁻¹. Due to the large size of the supercell, during atomic relaxations the Brillouin zone was sampled by the Γ point only.

For the STM calculations the single electron wave functions were calculated with a $3 \times 3 \times 1$ Γ -centered Monkhorst-Pack k-point mesh [22], and the revised Chen method [23] was used as implemented in the BSKAN code [24, 25]. According to this STM model the tunneling transmission ($|M|^2$) is calculated by a linear combination of spatial derivatives of the single electron wave functions (ψ) of the surface (graphene-metal in the present case) corresponding to the Chen's derivative rules [26] but also including tip-orbital interference effects. Two tip models were considered: (i) an *s*-wave tip orbital ($|M|^2 \sim |\psi|^2$) corresponding to the Tersoff–Hamann model [27], and (ii) an *s* + *p_z* tip orbital combination ($|M|^2 \sim |\psi + \partial\psi/\partial z|^2$) going beyond that. Due to the emerging *s* – *p_z* tip-orbital interference in the latter tip model, considerable STM contrast changes were reported in graphitic N-doped pure graphene (without metal support) depending on the *s* or *s* + *p_z* orbital composition of the model tips [23]. Whereas the *s* tip orbital in

the Tersoff–Hamann approximation is routinely used to model metallic tips, the $s + p_z$ tip is a good way to mimic oxygen-terminated functionalized tips as was demonstrated for STM imaging of molecules [28, 29]. On the experimental and simulated STM images, the brighter (darker) contrast indicates higher (lower) apparent height in constant-current mode.

3. Results and discussion

3.1. XPS measurements of N dopants

The presence of N dopants and their bonding configurations in the synthesized graphene materials have been examined by using XPS measurements based on the BE positions of N peaks [3, 6, 30–36]. Figures 1(a) and (b) are the XPS N 1s spectra measured on the graphene/Ir(111) and graphene/Ru(0001) surfaces prepared by using the sole precursor adenine. The BE of N dopants in graphene is in the range of 397.9–402.4 eV [37, 38], for which range the N 1s spectra in figure 1 show the clear existence of N dopants in graphene. It is worth mentioning that the N 1s peak is not obvious on our XPS survey spectra (see figure S1) as they were recorded using a single scan with a short dwell time. The BE ranges for three different substitutional doping configurations are 397.9–399.4 eV for pyridinic N, 399.3–400.5 eV for pyrrolic N, and 400.9–402.4 eV for graphitic N, respectively [37–39]. The N 1s spectra in figure 1, for the range of 397.9–402.4 eV, can be deconvoluted into three component peaks corresponding to the above mentioned three BE ranges. The BE range for pyrrolic N also covers another possible N bonding configuration nitrile N where a triple bond is formed between a nitrogen and a carbon atom [40]. Therefore, the component peak for this BE range is assigned as a mixture of pyrrolic N and nitrile N, and marked as pyrrolic/nitrile N in this study. Pyridinic N is bonded with two sp^2 -coordinated C atoms in a six-membered ring either at the graphene edge or next to a C vacancy inside the graphene lattice. Pyrrolic N is in a five-membered ring either at the graphene edge or next to a C vacancy inside the graphene lattice. Graphitic N substitutes the C atom in the graphene lattice and is bonded with three sp^2 -coordinated C atoms. As our N-doped graphene materials were annealed up to 1173 K or higher during the synthesis process, the N atoms of pyridinic N and graphitic N doping configurations are most likely not terminated with hydrogen due to completed dehydrogenation already achieved at temperatures lower than 623 K [41], and the amount of amino N is most likely negligible due to thermal instability above 1073 K [42]. In addition, previous studies show that the dehydrogenation of pyrrole occurs at 240 K [43], which suggests that most of pyrrolic N dopants, if any, are most likely not terminated with hydrogen in the grown materials.

Table 1 shows the fitting parameters for N 1s spectra including BE, area intensity and content percentage. The component peaks are all constrained to have full-width-half-maximum equal to 1.5 eV. The content percentage for each component peak is calculated by dividing the area intensity of this component peak by the total area intensity of all three component peaks. Among three component peaks, the graphitic N peak

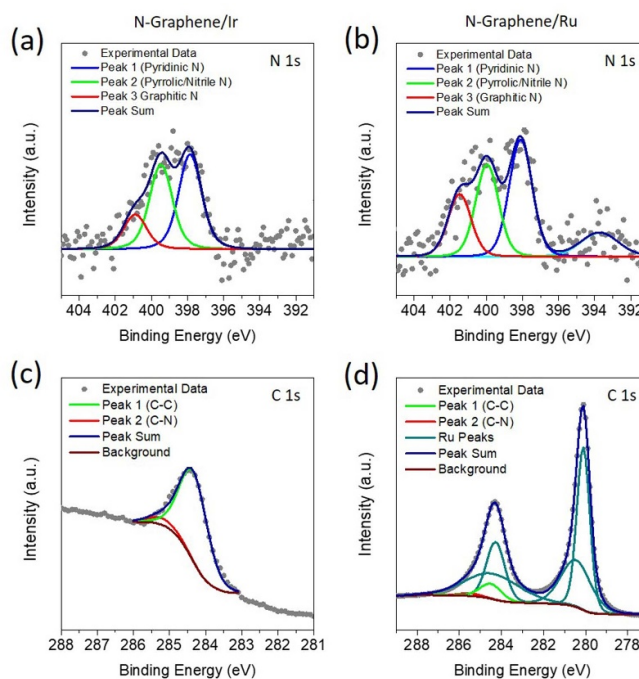


Figure 1. (a) and (b) XPS N 1s spectra of the N-doped graphene synthesized by using the sole precursor adenine on the (a) Ir(111) and (b) Ru(0001) surfaces. Spectra are obtained by subtracting linear background from raw data. The component peaks related to N dopants in graphene are pyridinic N (blue), pyrrolic/nitrile N (green), and graphitic N (red). (c) and (d) XPS C 1s spectra of the synthesized N-doped graphene on the (c) Ir(111) and (d) Ru(0001) surfaces. The Shirley background is used for both spectra. The Ru peaks in (d) were fitted based on the Ru 3d spectra measured on the bare Ru(0001) surface before graphene growth.

has the lowest content percentage and the pyridinic N peak has the highest content percentage for both N-graphene/Ir and N-graphene/Ru surfaces. Nonetheless, the XPS measurements confirm that N dopants have been successfully incorporated into the graphene layers.

The C 1s spectra of graphene/Ir and graphene/Ru are shown in figures 1(c) and (d) and the Shirley background is used for peak fitting. For graphene/Ir, the C 1s spectra in figure 1(c) can be deconvoluted into two different peaks centered at 284.3 eV and 285.2 eV. The peak centered at 284.3 eV can be assigned to sp^2 hybridized C atoms in graphene. The peak centered at 285.2 eV can be assigned to sp^2 hybridized C atoms bonded with N. For the C 1s spectra of graphene/Ru in figure 1(d), there is a very strong overlap between C 1s and Ru 3d energy ranges. The Ru 3d peaks are fitted based on the Ru 3d spectra measured on the bare Ru surface before graphene growth. The two C peaks centered at 284.5 eV and 285.5 eV are related to C–C and C–N, respectively.

3.2. Atomic-scale identification of N dopants in graphene by theoretical calculations and STM measurements

In the DFT calculations the metal-graphene slab geometry in the supercell is based on three metal Ir or Ru atomic layers of the substrate Ir(111) or Ru(0001) containing 9×9

Table 1. Fitting parameters for the deconvolution of XPS N 1s spectra.

	N-graphene/Ir			N-graphene/Ru		
	BE (eV)	Intensity	Percentage	BE (eV)	Intensity	Percentage
Pyridinic N	397.9	86.4	44.3%	398.1	124.1	43.1%
Pyrrolic/nitrile N	399.5	77.1	39.5%	400.0	97.6	33.9%
Graphitic N	400.9	31.5	16.2%	401.5	66.2	23.0%

Ir or 12×12 Ru atoms in each atomic layer, and the lattice constants of $a_{2D}^{\text{Ir}} = 2.74 \text{ \AA}$ [44] and $a_{2D}^{\text{Ru}} = 2.71 \text{ \AA}$ [45] were used. The metal substrate is followed by a single graphene overlayer in a 10×10 superstructure for Ir(111) and a 13×13 superstructure for Ru(0001), corresponding to the lattice mismatches between the metal and graphene. Altogether $443 = 3 \times 9 \times 9(\text{Ir}) + 2 \times 10 \times 10(\text{C})$ and $770 = 3 \times 12 \times 12(\text{Ru}) + 2 \times 13 \times 13(\text{C})$ atoms were included in the supercell, respectively, without nitrogen doping. The undoped relaxed metal-graphene structures showed good agreement with those reported in the literature [44–46]. We obtained a graphene layer corrugation of 0.29 \AA (1.38 \AA), and the closest carbon-metal atom distance is 3.36 \AA (2.25 \AA) for graphene/Ir (graphene/Ru).

N-doping configurations were considered as single graphitic N, pyridinic 1N, 2N and 3N, and single pyrrolic N defects at selected surface regions of the corrugated graphene layer, where the modeling is much more demanding than on a flat graphene layer on Ni(111) [47]. Graphitic N configurations were systematically calculated at (or close to) the highest and lowest position of the corrugated graphene layers. Correspondingly, in the following, graphitic N configurations where C is substituted by N (N_{C} defect) are denoted by $\text{GN}_{\text{high/low}}$, and pyridinic configurations containing $n = 1, 2, 3$ N atoms ($nN_{\text{C}}V_{\text{C}}$ complex) are denoted by PnN . As pyrrolic N bonding configurations could not be stabilized according to our DFT calculations (they always relaxed to pyridinic N defects), in the following, our atomic-scale identification of N dopants focuses on pyridinic N and graphitic N. For both metallic substrates GN_{high} is always energetically preferred compared to GN_{low} . In contrast, PnN is energetically preferred in the lower lying regions of the graphene sheet (that is why $PnN_{\text{high/low}}$ is not distinguished in our notation), and the reason is that the $nN_{\text{C}}V_{\text{C}}$ complex is stronger bound closer to the metal substrate. The considered $\text{GN}_{\text{high/low}}$ and PnN atomic configurations are shown in figure 2.

For N-doped graphene on Ir(111), five bonding configurations of N dopants have been considered in our DFT calculations, see the top row of figure 2, and two of them were often observed in our experimental STM measurements, including GN_{high} and P3N. Figure 3 shows the experimental and simulated STM images of GN_{high} and P3N. For the graphitic GN_{high} bonding configuration, at $+0.5 \text{ V}$, as shown in figures 3(a) and (b), the N atom is surrounded by six bright spots, three of which are much brighter than the other three. The three brighter spots correspond to the three six-membered rings containing the N dopant; and the other three spots correspond to the next-nearest three six-membered rings from the N dopant.

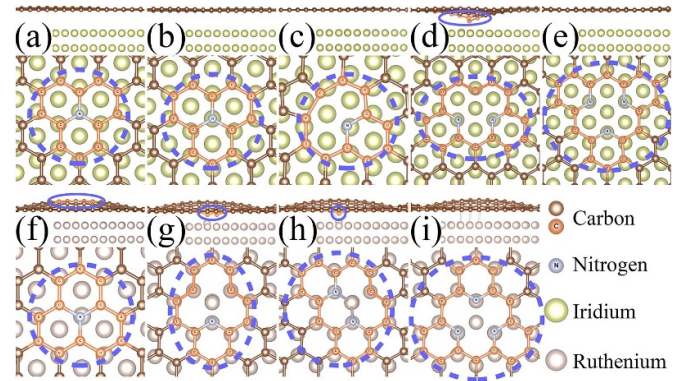


Figure 2. DFT-relaxed atomic structural models (side and top views) for N defects considered in this work: top row graphene/Ir(111): (a) GN_{high} , (b) GN_{low} , (c) P1N, (d) P2N, (e) P3N; bottom row graphene/Ru(0001): (f) GN_{high} , (g) P1N, (h) P2N, (i) P3N. The color coding of the atomic display is shown in the lower right panel. The carbon atoms closest to the N_{C} or $nN_{\text{C}}V_{\text{C}}$ ($n = 1, 2, 3$) defects are highlighted by orange color within the blue encircled regions.

This STM contrast resembles the one of graphitic-N on flat graphene without metal substrate [23]. At -0.5 V , as shown in figures 3(c) and (d), there is a dark depression at the N site and a slight brightness enhancement surrounding the N atom. This STM contrast is different from graphitic-N on flat free-standing graphene [23], and the reason might be metallic states contributing to the carbon sites surrounding the N atom. The features for graphitic N shown in figure 3 display a three-fold symmetry centered at the N site. The distinct difference between the STM contrasts of C and N atomic sites is caused by the large negative charge residing on the N atom, which was found to be 1.34 electrons in our case from Bader charge analysis. The pyridinic P3N defect, as shown in figures 3(e) and (f), is characterized by a triangular dark depression with a bright core and bright elevation along the edge of the triangle. The bright core is surrounded by three N atoms that are located in the depression. The main difference between images at $+0.05 \text{ V}$ and -0.05 V is the bright elevation along the edge of the triangle. Bader charge analysis resulted in negatively charged N atoms in the P3N defect with an average value of 1.09 excess electrons. These two types of defects discussed above were not observed for un-doped graphene/Ir samples. For the other three calculated configurations, in our STM measurements, we did not observe features on our samples that match well with the simulated STM images of GN_{low} and P1N, and occasionally observed a feature that is likely related to P2N (see figure S2). Note that the

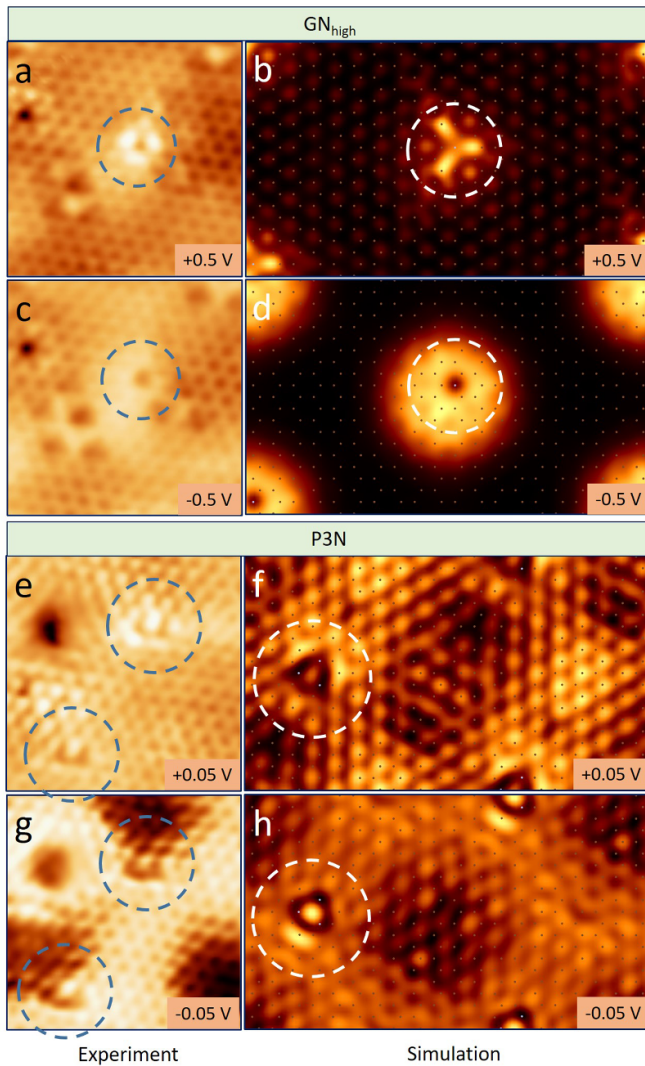


Figure 3. Experimental and simulated STM images of GN_{high} and P3N defects in N-doped graphene on Ir(111). The defects are marked with dashed circles. Scanning parameters: (a) $V_{\text{bias}} = +500 \text{ mV}$, $I = 5 \text{ nA}$; (c) $V_{\text{bias}} = -500 \text{ mV}$, $I = 5 \text{ nA}$; (e) $V_{\text{bias}} = +50 \text{ mV}$, $I = 1 \text{ nA}$; (g) $V_{\text{bias}} = -50 \text{ mV}$, $I = 5 \text{ nA}$. The apparent heights of the current contours in the simulations: (b) $\sim 3 \text{ \AA}$, (d) $\sim 2 \text{ \AA}$, (f) $\sim 5 \text{ \AA}$, (h) $\sim 6 \text{ \AA}$. On the simulated images, N and C atoms are represented by blue and brown dots, respectively. The size is $4.26 \text{ nm} \times 2.46 \text{ nm}$ for all simulated and $3 \text{ nm} \times 3 \text{ nm}$ for all experimental STM images.

best correspondence with the experimental STM images was obtained with an $s + p_z$ tip model employed in the STM simulations for N-doped graphene on Ir(111). This finding suggests the presence of a functionalized tip apex in these STM experiments.

Figure 4 shows two large scale STM images where the GN_{high} configuration is marked with blue arrows and the P3N configuration is marked with dashed green circles. The spatial distribution of N dopants in our graphene/Ir(111) samples is not uniform on the surface and varies with regions. In our extensive STM measurements, the graphitic GN_{high} configuration was observed much more often than the pyridinic P3N

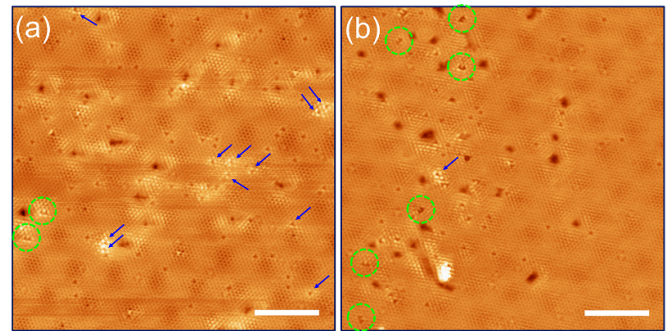


Figure 4. STM images of N-doped graphene on Ir(111). The pyridinic P3N defects are marked with dashed green circles and the graphitic GN_{high} defects are marked with blue arrows. Scanning parameters: (a) $V_{\text{bias}} = +500 \text{ mV}$, $I = 9 \text{ nA}$; (b) $V_{\text{bias}} = +50 \text{ mV}$, $I = 5 \text{ nA}$. Scale bars: (a) 4 nm and (b) 4 nm .

configuration in certain regions, like figure 4(a), and vice versa in other regions, like figure 4(b).

Figures 5 and 6 show STM images of N-doped graphene/Ru(0001) systems. Let us first focus on the description of the observed STM contrasts of the graphene/Ru outside the N defects. The main characteristic STM contrasts are the following at the given bias voltages shown in figure 5: The hilly region of graphene is imaged with the brightest contrast for both experiment and simulation. There is a secondary less pronounced bright contrast connecting the graphene hills (denoted by red circle in figure 5(e)). The simulated images show an enhanced rim and truncated triangular (hexagonal) shape of the graphene hills, whereas the experimental images show less truncated triangular shape for the same. Since the DFT-calculated graphene/Ru system exhibits hexagonal, i.e. truncated triangular shape for the graphene hill in the surface cell, the reason might be the different imaging conditions in the real experiment, e.g. tip effect. Apart from this, the main STM contrasts are the same for both experiment and simulation. Note that the enhanced rim of the graphene hill was also captured experimentally at a different tunneling condition, see figure 6(c).

Four bonding configurations of N dopants have been considered in our DFT calculations for N-doped graphene on Ru(0001), see the bottom row of figure 2. Two of the calculated configurations, GN_{high} and P3N, were often observed in our experimental STM measurements. Figure 5 shows the experimental and simulated STM images of GN_{high} and P3N. The main feature for GN_{high} is that the STM contrast at the N site is much brighter than its surrounding, as shown in figures 5(a)–(d) where the N site is indicated by an arrow. In addition, on the simulated images figures 5(b) and (d), N atoms are represented by blue dots. It is interesting to find that the GN_{high} defect appears bright, which is different than dark-appearing GN_{high} on weaker-corrugated graphene/Ir(111) (see figures 3(a)–(d)) and dark-appearing graphitic-N in flat graphene [23]. The reason is the carbon environment of the graphitic-N defect, which is much more curved for GN_{high} on the graphene hill of graphene/Ru than for graphene/Ir. Bader charge analysis

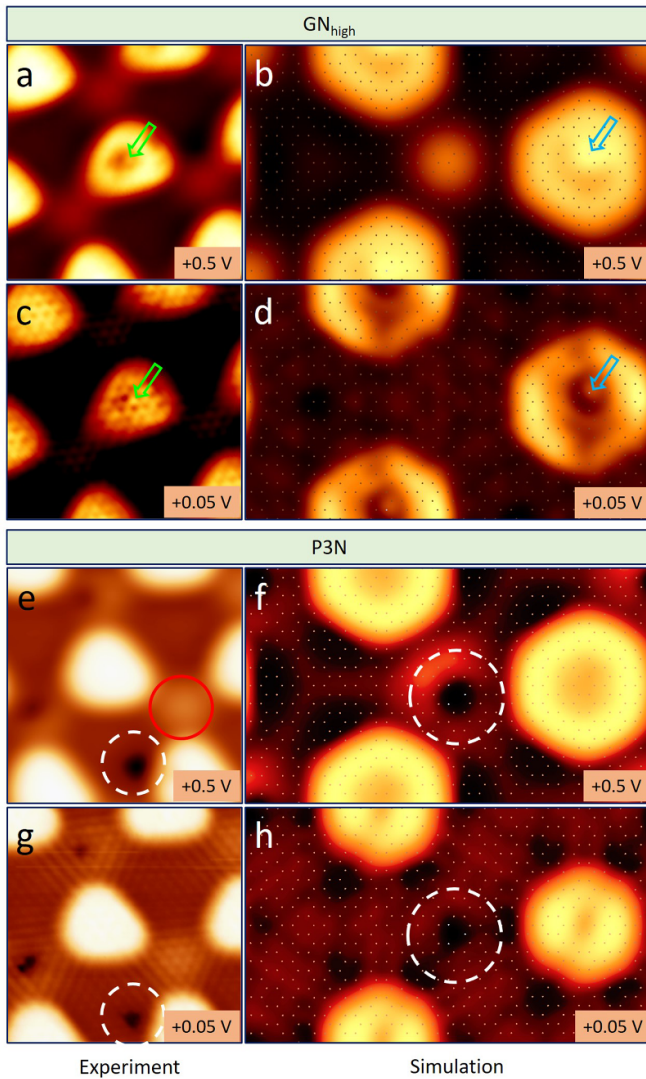


Figure 5. Experimental and simulated STM images of GN_{high} and P3N defects in N-doped graphene on Ru(0001). The defects are marked with arrows or dashed circles. Scanning parameters: (a) $V_{\text{bias}} = +500$ mV, $I = 1$ nA; (c) $V_{\text{bias}} = +50$ mV, $I = 1$ nA; (e) $V_{\text{bias}} = +500$ mV, $I = 1$ nA; (g) $V_{\text{bias}} = +50$ mV, $I = 9$ nA. The apparent heights of the current contours in the simulations: (b) ~ 2 Å, (d) ~ 6 Å, (f) ~ 6 Å, (h) ~ 2 Å. On the simulated images, N and C atoms are represented by blue and brown dots, respectively. The size is 4.26 nm \times 2.46 nm for all simulated and 5 nm \times 5 nm for all experimental STM images.

assigned 1.16 excess electrons to the N atom in the GN_{high} defect in graphene/Ru. For the STM image of P3N defect, it shows a rounded dark depression when the tip is far from the surface (at the high bias voltage and low current), as shown in figures 5(e) and (f); and it shows a triangular dark depression with a three-fold symmetry when the tip is close to the surface (at the low bias voltage and high current), as shown in figures 5(g) and (h). The three N atoms (with average excess electrons of 1.02 from Bader charge analysis), which are represented by blue dots in the simulated images in figures 5(f) and (h), are close to the edge of the rounded dark depression in figures 5(e) and (f) or the three corners of the triangular dark depression in figures 5(g) and (h). There is no bright elevation

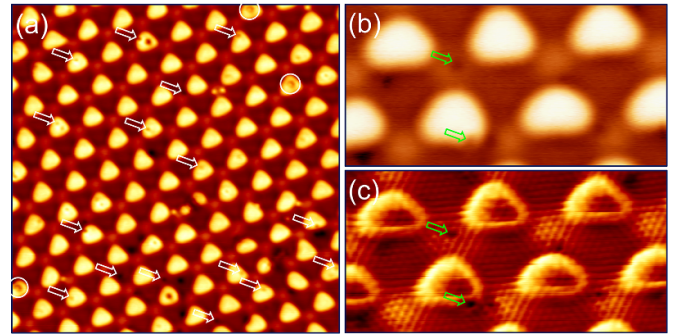


Figure 6. STM images of N-doped graphene on Ru(0001). The graphitic GN_{high} defects are marked with white circles. The white arrows in (a) indicate some possible sites for pyridinic P3N defects. The green arrows in (b) and (c) indicate two P3N defects. The two images, (b) and (c), were recorded in the same region. Scanning parameters: (a) $V_{\text{bias}} = +1$ V, $I = 50$ pA, size: 29 nm \times 29 nm; (b) $V_{\text{bias}} = +500$ mV, $I = 50$ pA, size: 10 nm \times 5 nm; (c) $V_{\text{bias}} = +10$ mV, $I = 50$ pA, Size: 10 nm \times 5 nm.

at the edge of the triangular dark depression, as shown in figures 5(g) and (h). There is no bright elevation at the edge of the rounded dark depression on the experimental image in figure 5(e); and the bright elevation on the upper side of the rounded dark depression on the simulated image in figure 5(f) is a feature that also exists on the un-doped graphene/Ru(0001) surface, see the red solid circle in figure 5(e). The two types of defects discussed above were not observed for un-doped graphene/Ru samples. For the other two calculated configurations, we did not observe features on our samples that match well with the simulated STM images of P1N and occasionally observed a feature that is likely related to P2N (see figure S3). Note that the best correspondence with the experimental STM images was obtained with an s tip model employed in the STM simulations for N-doped graphene on Ru(0001). This finding suggests the presence of a metal tip apex in these STM experiments.

As seen in figure 6(a), in our STM measurements, the observed amount of P3N defects is greater than GN_{high} defects within the graphene sheet on our graphene/Ru samples, which is in agreement with the XPS results in figure 1. The GN_{high} defects are marked with white circles in figure 6(a). There are many dark spots on the surface and some of them are marked with white arrows in figure 6(a) as examples. Our extensive STM measurements indicate that about half of the dark spots, like the two defects marked in figures 6(b) and (c), are imaged as rounded dark depression at $+0.5$ V, and as triangular dark depressions at low bias voltages ($+0.01$ – 0.05 V), which is the feature for the P3N defect (see also figures 5(e)–(h)).

It is interesting to mention that, in our STM measurements, the spatial distribution of N defects is more uniform on the graphene/Ru(0001) surface than on the graphene/Ir(111) surface, as shown in figure S4, although the same sole precursor and growth conditions were used on these two different metal surfaces. Another interesting point is that the best correspondence with the experimental STM images was obtained with an $s + p_z$ tip orbital combination employed in the STM simulations for N-doped graphene/Ir(111), and an s tip orbital for

graphene/Ru(0001). This suggests that the tip conditions are different in the STM experiments of these two separate systems, and due to our experimental experience the metal tip gets easily functionalized at high tunneling currents, even during scanning.

4. Conclusions

In summary, we have investigated the bonding configurations of N dopants in corrugated graphene on the Ru(0001) and Ir(111) surfaces synthesized using the sole precursor adenine. XPS measurements indicate the existence of multiple different doping configurations in the synthesized graphene materials. By combining DFT calculations and STM measurements, we have identified graphitic and pyridinic N dopants in the corrugated graphene layers on the atomic scale. Negatively charged graphitic-N and pyridinic-3N defects were found the most abundant, and their STM appearance was studied. Importantly, we report STM contrast changes of graphitic-N defects depending on the local curvature of the surrounding carbon sheet in the close vicinity of the nitrogen atom. This study provides valuable atomic-scale information for the bonding configurations of N dopants in corrugated graphene prepared using a sole precursor, which are helpful to the design, fabrication and application of doped rippled graphene materials.

Data availability statement

The data cannot be made publicly available upon publication because they are not available in a format that is sufficiently accessible or reusable by other researchers. The data that support the findings of this study are available upon reasonable request from the authors.

Acknowledgments

We gratefully acknowledge the financial supports from National Science Foundation (NSF) (Grants Nos. DMR-1809805 and DMR-1828019), National Research Development and Innovation Office of Hungary (NKFIH, Grants Nos. FK124100 and K138714), and California State University Northridge. I A acknowledges a Stipendium Hungaricum Scholarship of the Tempus Public Foundation. K P acknowledges the János Bolyai Research Grant of the Hungarian Academy of Sciences (Grant No. BO/292/21/11) and the New National Excellence Program of the Ministry for Innovation and Technology from NKFIH Fund (Grant No. ÚNKP-22-5-BME-282). H Y and H J G acknowledge support from National Natural Science Foundation of China (Grant No. 61888102) and National Key Research and Development Program of China (Grant No. 2019YFA0308500). The XPS measurements were performed on an instrument acquired with financial support from the U.S. Army Research Office (Contract #: W911NF-17-1-0459).

ORCID iD

Krisztián Palotás  <https://orcid.org/0000-0002-1914-2901>

References

- [1] Wang X, Sun G, Routh P, Kim D-H, Huang W and Chen P 2014 Heteroatom-doped graphene materials: syntheses, properties and applications *Chem. Soc. Rev.* **43** 7067–98
- [2] Narita A, Wang X Y, Feng X and Müllen K 2015 New advances in nanographene chemistry *Chem. Soc. Rev.* **44** 6616–43
- [3] Wang H, Maiyalagan T and Wang X 2012 Review on recent progress in nitrogen-doped graphene: synthesis, characterization, and its potential applications *ACS Catal.* **2** 781–94
- [4] Ito Y, Christodoulou C, Nardi M V, Koch N, Kläui M, Sachdev H and Müllen K 2015 Tuning the magnetic properties of carbon by nitrogen doping of its graphene domains *J. Am. Chem. Soc.* **137** 7678–85
- [5] Shan J, Liu Y, Liu P, Huang Y, Su Y, Wu D and Feng X 2015 Nitrogen-doped carbon-encapsulated SnO₂-SnS/graphene sheets with improved anodic performance in lithium ion batteries *J. Mater. Chem. A* **3** 24148–54
- [6] Reddy A L M, Srivastava A, Gowda S R, Gullapalli H, Dubey M and Ajayan P M 2010 Synthesis of nitrogen-doped graphene films for lithium battery application *ACS Nano* **4** 6337–42
- [7] Yang Z, Nie H, Chen X A, Chen X and Huang S 2013 Recent progress in doped carbon nanomaterials as effective cathode catalysts for fuel cell oxygen reduction reaction *J. Power Sources* **236** 238–49
- [8] Zabet-Khosousi A, Zhao L, Pálová L, Hybertsen M S, Reichman D R, Pasupathy A N and Flynn G W 2014 Segregation of sublattice domains in nitrogen-doped graphene *J. Am. Chem. Soc.* **136** 1391–7
- [9] Neilson J *et al* 2019 Nitrogen-doped graphene on copper: edge-guided doping process and doping-induced variation of local work function *J. Phys. Chem. C* **123** 8802–12
- [10] Joucken F *et al* 2012 Localized state and charge transfer in nitrogen-doped graphene *Phys. Rev. B* **85** 161408(R)
- [11] Tison Y *et al* 2015 Electronic interaction between nitrogen atoms in doped graphene *ACS Nano* **9** 670–8
- [12] Telychko M, Mutombo P, Ondráček M, Hapala P, Bocquet F C, Kolorenč J, Vondráček M, Jelinek P and Švec M 2014 Achieving high-quality single-atom nitrogen doping of graphene/SiC(0001) by ion implantation and subsequent thermal stabilization *ACS Nano* **8** 7318–24
- [13] Lv R *et al* 2012 Nitrogen-doped graphene: beyond single substitution and enhanced molecular sensing *Sci. Rep.* **2** 586
- [14] Cress C D, Schmucker S W, Friedman A L, Dev P, Culbertson J C, Lyding J W and Robinson J T 2016 Nitrogen-doped graphene and twisted bilayer graphene via hyperthermal ion implantation with depth control *ACS Nano* **10** 3714–22
- [15] Zhao L *et al* 2011 Visualizing individual nitrogen dopants in monolayer graphene *Science* **333** 999–1003
- [16] Fiori S, Perilli D, Panighel M, Cepek C, Ugolotti A, Sala A, Liu H, Comelli G, Valentin C D and Africh C 2021 ‘Inside out’ growth method for high-quality nitrogen-doped graphene 2021 *Carbon* **171** 704–10
- [17] Kresse G and Furthmüller J 1996 Efficient iterative schemes for *ab initio* total-energy calculations using a plane-wave basis set *Phys. Rev. B* **54** 11169–86

- [18] Kresse G and Furthmüller J 1996 Efficiency of *ab-initio* total energy calculations for metals and semiconductors using a plane-wave basis set *Comput. Mater. Sci.* **6** 15–50
- [19] Kresse G and Joubert D 1999 From ultrasoft pseudopotentials to the projector augmented-wave method *Phys. Rev. B* **59** 1758–75
- [20] Klimeš J, Bowler D R and Michaelides A 2010 Chemical accuracy for the van der Waals density functional *J. Phys.: Condens. Matter* **22** 022201
- [21] Klimeš J, Bowler D R and Michaelides A 2011 Van der Waals density functionals applied to solids *Phys. Rev. B* **83** 195131
- [22] Monkhorst H J and Pack J D 1976 Special points for Brillouin-zone integrations *Phys. Rev. B* **13** 5188–92
- [23] Mándi G and Palotás K 2015 Chen’s derivative rule revisited: role of tip-orbital interference in STM *Phys. Rev. B* **91** 165406
- [24] Hofer W A 2003 Challenges and errors: interpreting high resolution images in scanning tunneling microscopy *Prog. Surf. Sci.* **71** 147–83
- [25] Palotás K and Hofer W A 2005 Multiple scattering in a vacuum barrier obtained from real-space wavefunctions *J. Phys.: Condens. Matter* **17** 2705–13
- [26] Chen C J 1990 Tunneling matrix elements in three-dimensional space: the derivative rule and the sum rule *Phys. Rev. B* **42** 8841–57
- [27] Tersoff J and Hamann D R 1985 Theory of the scanning tunneling microscope *Phys. Rev. B* **31** 805–13
- [28] Gross L, Moll N, Mohn F, Curioni A, Meyer G, Hanke F and Persson M 2011 High-resolution molecular orbital imaging using a *p*-wave STM tip *Phys. Rev. Lett.* **107** 086101
- [29] Siegert B, Donarini A and Grifoni M 2013 The role of the tip symmetry on the STM topography of π -conjugated molecules *Phys. Status Solidi b* **250** 2444–51
- [30] Akada K, Terasawa T O, Imamura G, Obata S and Saiki K 2014 Control of work function of graphene by plasma assisted nitrogen doping *Appl. Phys. Lett.* **104** 131602
- [31] Li X, Wang H, Robinson J T, Sanchez H, Diankov G and Dai H 2009 Simultaneous nitrogen doping and reduction of graphene oxide *J. Am. Chem. Soc.* **131** 15939–44
- [32] Shao Y, Zhang S, Engelhard M H, Li G, Shao G, Wang Y, Liu J, Aksay I A and Lin Y 2010 Nitrogen-doped graphene and its electrochemical applications *J. Mater. Chem.* **20** 7491–6
- [33] Sheng Z H, Shao L, Chen J J, Bao W J, Wang F B and Xia X H 2011 Catalyst-free synthesis of nitrogen-doped graphene via thermal annealing graphite oxide with melamine and its excellent electrocatalysis *ACS Nano* **5** 4350–8
- [34] Miao Q, Wang L, Liu Z, Wei B, Xu F and Fei W 2016 Magnetic properties of N-doped graphene with high curie temperature *Sci. Rep.* **6** 21832
- [35] Joucken F et al 2015 Charge transfer and electronic doping in nitrogen-doped graphene *Sci. Rep.* **5** 14564
- [36] Schiros T et al 2012 Connecting dopant bond type with electronic structure in N-doped graphene *Nano Lett.* **12** 4025–31
- [37] Vesel A, Zaplotnik R, Primc G and Mozetič M 2020 A review of strategies for the synthesis of N-doped graphene-like materials *Nanomaterials* **10** 2286
- [38] Lazar P, Mach R and Otyepka M 2019 Spectroscopic fingerprints of graphitic, pyrrolic, pyridinic, and chemisorbed nitrogen in N-doped graphene *J. Phys. Chem. C* **123** 10695–702
- [39] Lai L F, Potts J R, Zhan D, Wang L, Poh C K, Tang C H, Gong H, Shen Z X, Lin J Y and Ruoff R S 2012 Exploration of the active center structure of nitrogen-doped graphene-based catalysts for oxygen reduction reaction *Energy Environ. Sci.* **5** 7936–42
- [40] Hellgren N, Haasch R T, Schmidt S, Hultman L and Petrov I 2016 Interpretation of x-ray photoelectron spectra of carbon-nitride thin films: new insights from *in situ* XPS *Carbon* **108** 242–52
- [41] Späth F, Zhao W, Gleichweit C, Gotterbarm K, Bauer U, Höfert O, Steinrück H P and Papp C 2015 Hydrogenation and dehydrogenation of nitrogen-doped graphene investigated by x-ray photoelectron spectroscopy *Surf. Sci.* **634** 89–94
- [42] Zhang C, Hao R, Liao H and Hou Y 2013 Synthesis of amino-functionalized graphene as metal-free catalyst and exploration of the roles of various nitrogen states in oxygen reduction reaction *Nano Energy* **2** 88–97
- [43] Papp C 2007 *In-situ* investigations of adsorbed hydrocarbons—model systems of heterogeneous catalysis *PhD Thesis* University of Erlangen-Nuremberg
- [44] Pacilé D et al 2013 Artificially lattice-mismatched graphene/metal interface: graphene/Ni/Ir(111) *Phys. Rev. B* **87** 035420
- [45] Alfè D et al 2013 Fine tuning of graphene-metal adhesion by surface alloying *Sci. Rep.* **3** 2430
- [46] Moritz W, Wang B, Bocquet M L, Brugger T, Greber T, Wintterlin J and Günther S 2010 Structure determination of the coincidence phase of graphene on Ru(0001) *Phys. Rev. Lett.* **104** 136102
- [47] Ma C, Liao Q, Sun H, Lei S, Zheng Y, Yin R, Zhao A, Li Q and Wang B 2018 Tuning the doping types in graphene sheets by N monoelement *Nano Lett.* **18** 386–94